Research Square

Preprints are preliminary reports that have not undergone peer review.
They should not be considered conclusive, used to inform clinical practice,
or referenced by the media as validated information.

Distribution Characteristics and Controlling Mechanisms of Radon and Primordial Radionuclides in a Certain Impact Crater in China

Zhiqiang LIU
Heilongjiang Institute of Atomic Energy
Yan SHI
Heilongjiang Institute of Atomic Energy
Wanshan LEI
School of Earth Scienceand Resources, Chang'an University
Zhiwei WANG
State Key Laboratory of Coal Mine Disaster Dynamics and Control
Gang YAO
Heilongjiang Institute of Atomic Energy
Wa GAO
gw_6019@163.com
Heilongjiang Institute of Atomic Energy

Research Article

Keywords: Impact crater, Radon (222Rn), Natural radionuclides, Sediment, Granite

Posted Date: July 27th, 2026

DOI: https://doi.org/10.21203/rs.3.rs-10350133/v1

License: This work is licensed under a Creative Commons Attribution 4.0 International License.
Read Full License

Additional Declarations: No competing interests reported.

Distribution Characteristics and Controlling Mechanisms of Radon and Primordial Radionuclides in a Certain Impact Crater in China

Zhi-qiang LIU [1], Yan SHI[1,2], Wan-shan LEI [3], Zhi-wei WANG[4], Gang YAO[1], Wa GAO[1*]

[1] Heilongjiang Institute of Atomic Energy，Harbin，150086,China

[2] College of Nuclear Science and Technology, Harbin Engineering University，Harbin，15000,China

[3]School of Earth Scienceand Resources, Chang'an University, Xi' an, Shaanxi 710054,China

[4] State Key Laboratory of Coal Mine Disaster Dynamics and Control, Chongqing University, Chongqing 400044, China

E-mail address of the corresponding author: gw_6019@163.com

Abstract

To reveal the controlling mechanism of impact structure on the spatial distribution of radon and primordial natural radionuclides and provide basic data for planetary geological research, systematic field sampling and laboratory analyses were conducted at a certain impact crater in China. A high-purity germanium (HPGe) γ -ray spectrometer and scintillation-cell radon detector were adopted to measure the activity concentrations of

^{232}Th, ^{40}K and gaseous ^{222}Rn in granite, surface sediment and ambient air across 11 sampling sites covering crater core, crater rim and outer rim zones. The results indicated obvious spatial differentiation of target radionuclides following the sequence: granite > sediment and inner rim > outer rim. The measured specific activities of ^{40}K and ^{232}Th fell within the global natural background range, jointly governed by parent rock lithology, impact-induced rock fragmentation, weathering leaching as well as coupled topography and hydrological conditions. Radon concentration exhibited a distinct spatial pattern with high values concentrated in crater core and decreasing towards peripheral areas, and sediment was identified as the dominant radon reservoir within the study area. Radon concentrations in surface water remained low, indicating limited radiological risk under the measured conditions.. This study clarifies the spatial distribution patterns and controlling mechanisms of natural radioactivity for granite-hosted impact craters in frigid-temperate regions, supplying fundamental datasets and technical support for radiation risk evaluation and element cycling research of planetary impact geology.

Keywords Impact crater; Radon (^{222}Rn); Natural radionuclides; Sediment; Granite

Introduction

The spatial distribution and formation mechanisms of ^{222}Rn and primordial radionuclides, such as ^{232}Th and ^{40}K, are important indicators for assessing regional radiation environments and geological evolution in impact craters, mineralized areas, and building-material regions. [1,2]. A certain impact crater in China is one of the largest known terrestrial impact structures formed within the past 100,000 years [3]. Its unique geological setting and evolutionary history endow the local natural radionuclide distribution with particular characteristics apart from general rules of terrestrial impact structures.

As a gaseous decay progeny of ^{226}Ra with a half-life of 3.82 d, ^{222}Rn concentration is tightly correlated with the spatial occurrence of precursor ^{226}Ra and permeability of host geological media[4]. Radon originates from spontaneous radioactive decay of ^{238}U hosted in granite, sediment and aquifer water and readily accumulates in confined geological voids. Global extensive field surveys on radon and associated primordial radionuclides have been conducted to quantify environmental radon exposure risks in different regions[5,6]. Previous studies have also examined the hydrogeochemical behavior of aqueous radon and the abundance of natural radioelements in granitic terrains. [7,8]. As a well-preserved terrestrial impact structure in China, detailed radioelement investigation of the studied crater provides new insights into elemental geochemical migration under cold-climate geological settings.

Formed via asteroid hypervelocity impact, impact craters possess unique geological architectures featured by intensely fractured granite, pervasive fracture networks, mineral phase transformation and element redistribution. Such post-impact modifications alter the original occurrence modes of in-situ primordial radionuclides and construct favorable migration pathways for radon generation and exhalation, making crater-scale investigations of radionuclides and radon important for planetary geology and environmental geochemistry. Geologically, the studied crater is a verified terrestrial impact structure in China following

Xiuyan crater[3,9], developed on Cretaceous granite basement overlain by heavily fractured breccia and dense fracture systems generated during impact excavation, which theoretically facilitates radon production and subsurface migration. Although existing studies have reported preliminary data on natural radioactivity in several typical impact craters worldwide[10,11], systematic field investigations of radon and primordial radionuclide distributions, together with their controlling factors, remain limited for cold-climate granitic impact craters.

A certain impact crater in China acts as an in-situ natural laboratory to decipher element cycling and subsurface gas migration driven by hypervelocity impact events. In this work, field monitoring of radon concentration in granite, soil, surface water and ambient air was carried out systematically covering core, eastern, western, southern, northern rim and outer peripheral zones, accompanied by quantitative γ -spectroscopic determination of background activity of ^{40}K and ^{232}Th. Spatial distribution contour maps of target radionuclides and radon were plotted to clarify the control of impact tectonics on natural radioelement enrichment, providing a scientific basis for radiation environmental assessment and the protection of crater geological resources.

Geological Setting and Methods

Geological Setting

A certain impact crater in China was formed approximately 49 ka ago by a meteorite impact and is located in a region characterized by a mid-temperate continental monsoon climate[3]. Tectonically situated in the eastern part of the East Asian Orogenic Belt, the region underwent intensive tectono-magmatic activity since the late Neoproterozoic, dominated by Permian and Cretaceous granites overlain by multi-stage sedimentary sequences spanning from the Neoproterozoic to the Quaternary[3]. Geophysical inversion suggests that the original crater diameter is approximately 1.85 km; the crater is characterized by an incomplete annular uplifted rim surrounding a flat central depression with steep inner rim slopes (Fig.1).

Crater rim is predominantly composed of loose granitic clastics and breccia deposits, while central depression is filled with lacustrine sediment, granitic breccia and gravel covered by 30-90 cm dark brown topsoil. Within 200 m adjacent to crater wall, subsurface lithology consists of fractured granite breccia; the central ~1 km diameter core area is underlain by clayey lacustrine deposits including silty clay and fine sand with underlying granitic breccia sequences confirmed via stratigraphic contact relationships[3].

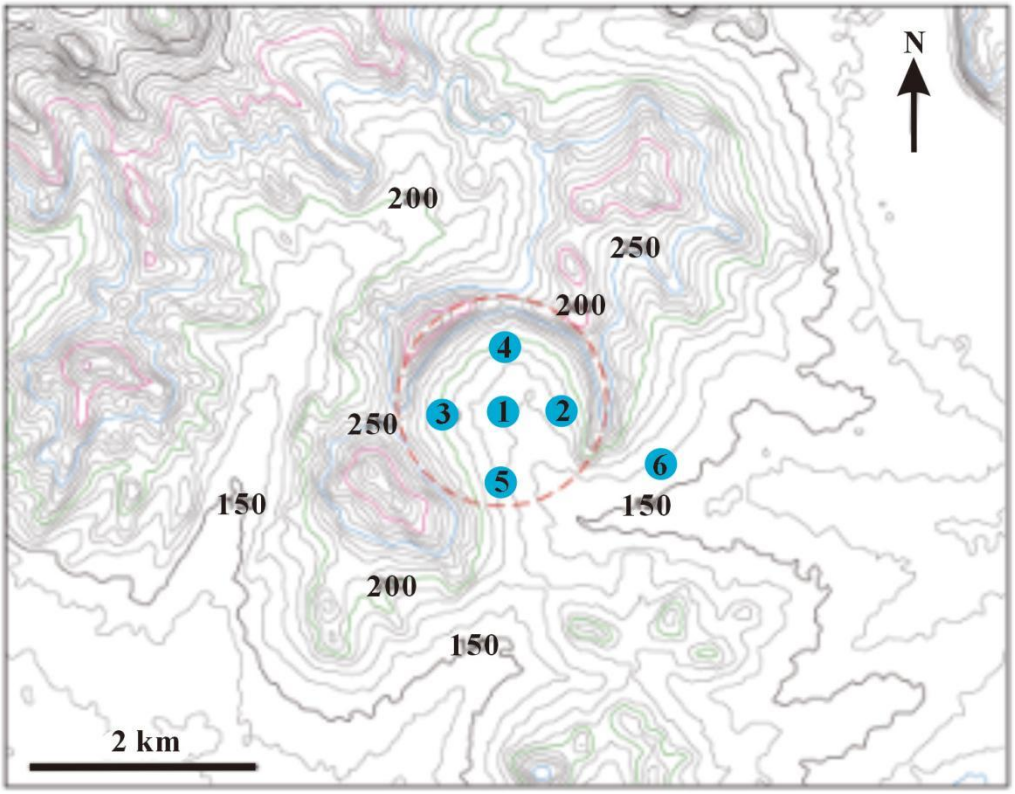


Figure 1 Geological background map of a certain impact crater in China

(Figure1）①:Sampling Sites for Radionuclides in Granite and Sediments of the Impact Crater Core, and Radon Concentrations in Air and Soil；②:Sampling Sites for Radionuclides in Granite and Sediments of the Eastern Impact Crater Rim, and Radon Concentrations in Air and Soil；③:Sampling Sites for Radionuclides in Granite and Sediments of the Western Impact Crater Rim, and Radon Concentrations in Air and Soil;④:Sampling Sites for Radionuclides in Granite of the Northern Impact Crater Rim, and Radon Concentrations in Air, Soil and Surface Water;⑤:Sampling Sites for Radionuclides in Granite and Sediments of the Southern Impact Crater Rim, and Radon Concentrations in Air, Soil and Surface Water;⑥:Sampling Sites for Radionuclides in Granite and Sediments Outside the Impact Crater Rim)

Sampling and Analytical Instruments

Sample Collection

Eleven solid samples (0-20 cm depth) of granite and surficial sediment were collected from core, four directional rim sites and outer rim for γ-spectrometric radionuclide analysis; meanwhile, twelve in-situ measurements of soil gas radon, atmospheric radon and surface water radon were performed at core and four directional rim locations (Fig.1). A After field collection, the solid samples were crushed in the laboratory with individual sample mass ranging from 0.214 kg to 0.349 kg (average: 0.322 kg).

Radon Measurement via Scintillation Cell Detector

FD216 scintillation-type radon monitor was used to quantify radon activity in soil gas, ambient air and surface water based on linear positive correlation between pulse count rate and radon volumetric activity. Duplicate measurements were performed at each of the five sampling locations (core, N/S/E/W rim).For soil radon detection: a 80 cm-long steel probe (Φ=2.0 cm) was drilled down to ~70 cm subsurface, sampling probe was rapidly inserted and sealed after probe withdrawal, connected to detector via rubber tube; operational parameters: gas filling 2 min, measurement 5 min, gas exhaust 2 min under dedicated soil radon mode.For atmospheric radon measurement: instrument preheated $\geqslant$30 min onsite, parameters set as 10 min gas intake, 20 min measurement and 1 min exhaust.For aqueous radon analysis: 400 mL water sampling bottle coupled with detector after 15 min preheating under liquid radon mode, sequentially subjected to background counting (10min), gas extraction (5min), formal measurement (11min) and gas discharge (5min). The FD216 detector is annually calibrated by National Institute of Metrology, China following JJG825-2013 specification to guarantee testing repeatability and measurement precision.

HPGe γ -Ray Spectrometry for ^{232}Th and ^{40}K

Specific activities of ^{232}Th and ^{40}K in granite and sediment specimens were quantified using GEM30P4-76 HPGe γ -spectrometer with continuous counting duration of 24 h per sample. The analytical system is composed of high-purity germanium crystal detector, signal processing module and multi-channel buffer (MCB) supported by specialized spectral analysis software capable of background subtraction and peak deconvolution. Characteristic γ -peaks at 583.2 keV (^{208}Tl, decay progeny of ^{232}Th), 911.2 keV (^{228}Ac) and 1460.8 keV (^{40}K) were adopted for quantitative calculation with unit of Bq • kg^{-1}. The detector is shielded by combined lead-iron barrier to eliminate environmental background interference and calibrated yearly by National Institute of Metrology, China in accordance with JJF 1850-2020 calibration standard for germanium γ -spectrometers.

Data Processing

In-situ radon readings were recorded directly during fieldwork (Table 1). Both ^{232}Th and ^{40}K belong to long-lived primordial radionuclides with half-lives far exceeding the time interval between sampling and laboratory measurement; radioactive equilibrium maintains between parent ^{232}Th and its daughter nuclides (^{208}Tl, ^{228}Ac), hence decay correction coefficient was approximated as unity. The average activity of ^{232}Th was calculated from dual daughter peak results referring to Chinese standard GB/T 16145-2022 (Formula 1). Spatial distribution contour maps of radon, ^{232}Th and ^{40}K were generated via spatial interpolation with Python Matplotlib and Scipy modules (Fig.2,Fig.4).

$$A_b = \frac{(N_S/T_S - N_b/T_b)}{F_2 \varepsilon P m e^{-\lambda \Delta t}} F_1 F_3 \quad (1)$$

A_b：Activity concentration of radionuclides in samples at sampling time, unit: becquerel per kilogram (Bq/kg)；Ns：Net count of full-energy peak area for sample measurement； Ts：Live time of sample measurement, unit: second (s)；N_b：Net count of background peak area ；T_b：Live time of background measurement, unit: second (s)；F_1：Decay correction factor for short-lived radionuclides during measurement. If the half-life of the target radionuclide is more than 100 times the sample measurement duration, F_1 is set to 1. F_2 is adopted as 1 in the data calculation of this study；F_2：Gamma self-absorption correction factor of samples relative to efficiency calibration standard sources. F_2 is taken as 1 when the density of the sample is similar to that of the calibration source, and F_2 is set to 1 in this study；F_3：Gamma coincidence summing correction factor. For radionuclides emitting single-energy gamma rays or cases with negligible correction for the target gamma rays, F_3 is set to 1; otherwise, F_3 shall be calculated. F_3 is adopted as 1 in this study；ε： Full-energy peak detection efficiency of gamma rays at corresponding energy, unit: count rate per becquerel [(count/s)/Bq]； P：Emission branching ratio of gamma rays at corresponding energy；m：Mass or volume of the measured sample, unit: kilogram (kg)； e： Natural constant； λ： Decay constant of radionuclides, unit: reciprocal second (s^{-1})；Δt：Radionuclide decay time, i.e., the time interval from sampling to sample measurement, unit: second (s).

Results and Discussion

Spatial Distribution of Radon Concentration in a Certain Impact Crater in China

Spatial Differentiation of In-situ Radon

Radon concentration follows the descending order: Crater core > East rim > West rim > South rim > North rim (Table 1). The average radon activity in sediment and ambient air reaches the maximum at crater core (35799.5 Bq/m^3 for sediment, 1655.1 Bq/m^3 for air), while minimum values occur at north rim (61.3 Bq/m^3, 80.6 Bq/m^3). Within identical sampling location, sediment always contains remarkably higher radon than overlying atmosphere, whereas surface water radon remains negligible (4.5 Bq/m^3 at north rim, 1.2 Bq/m^3 at south rim), lower than average groundwater radon (8.1 Bq/L^3) in Greater Accra Region of Ghana and complying with WHO drinking water radon threshold [14], verifying sediment as dominant radon storage medium within the crater system.

Table 1 Radon concentrations in a certain impact crater in China

Sampling area	Soil-gas radon (Bq/m³)	Surface-water radon (Bq/m³)	Atmospheric radon (Bq/m³)	Mean soil-gas radon (Bq/m³)	Mean atmospheric radon (Bq/m³)
North rim	71.7 50.8	4.5 1.2	90.3 70.8	61.3	80.6
South rim	300.0 174.6		107.1 247.1	237.3	177.1
East rim	4772.4 56.7		385.8 522.4	2414.6	454.1
West rim	361.0 283.5		98.6 125.1	322.3	111.9
Crater core	38661.8 32937.1		2232.2 1077.9	35799.5	1655.1

Cross-regional comparison of radon levels is summarized in Table 2. The average soil-gas radon concentration of the studied crater (8220 Bq/m^3) is lower than the peak soil-gas radon concentration reported in Shizuishan, Ningxia (54000.6 Bq/m^3)[15] and the soil-gas radon concentration at Kilbourne Hole Maar, USA (15000 Bq/m^3)[16]. The mean atmospheric radon concentration in the studied crater (496 Bq/m^3) is higher than the average mine-air radon

concentration reported in Figueira, Brazil (227 Bq/m^3)[18]. The Croatian cellar data listed in Table 2 represent cumulative radon exposure rather than instantaneous concentration and are therefore used only as a reference for high-radon confined environments [17]. The measured surface-water radon is significantly below drinking-water radon around Rafsanjan Fault, Iran (18.480Bq/L) and thermal spring water of Yalova Basin, Turkey (2.4Bq/L) [19,20], demonstrating low-level aqueous radon across the research area. Interpolated contour maps (Fig. 2) display a concentric decreasing trend of both air and soil-gas radon from the central high-value zone outward, controlled jointly by crater topography and host lithology; high soil-gas radon (>35000 Bq/m^3) and atmospheric radon (>1700 Bq/m^3) are concentrated in the core depression, indicating a sediment reservoir effect.

Table 2 Comparison of radon levels in a certain impact crater in China and other regions

Region / environment	Soil-gas radon	Water radon	Air radon / cumulative exposure	Unit
A certain impact crater in China	8220.0	2.0	496.0	Bq/m³
Shizuishan, Ningxia, China [15]	54006.6	—	—	Bq/m³
Kilbourne Hole Maar, USA [16]	15000.0	—	—	Bq/m³
Cellars during the Croatian war [17]	—	—	$(6.62 \pm 3.17) \times 10^4$	Bq·h/m³
Figueira mine, Brazil [18]	—	—	227.0	Bq/m³
Drinking water near the Rafsanjan Fault, Iran [19]	—	18.5	—	Bq/L
Thermal spring water in the Yalova Basin, Turkey [20]	—	2.4	—	Bq/L

Note: The Croatian cellar value represents cumulative radon exposure rather than instantaneous concentration.

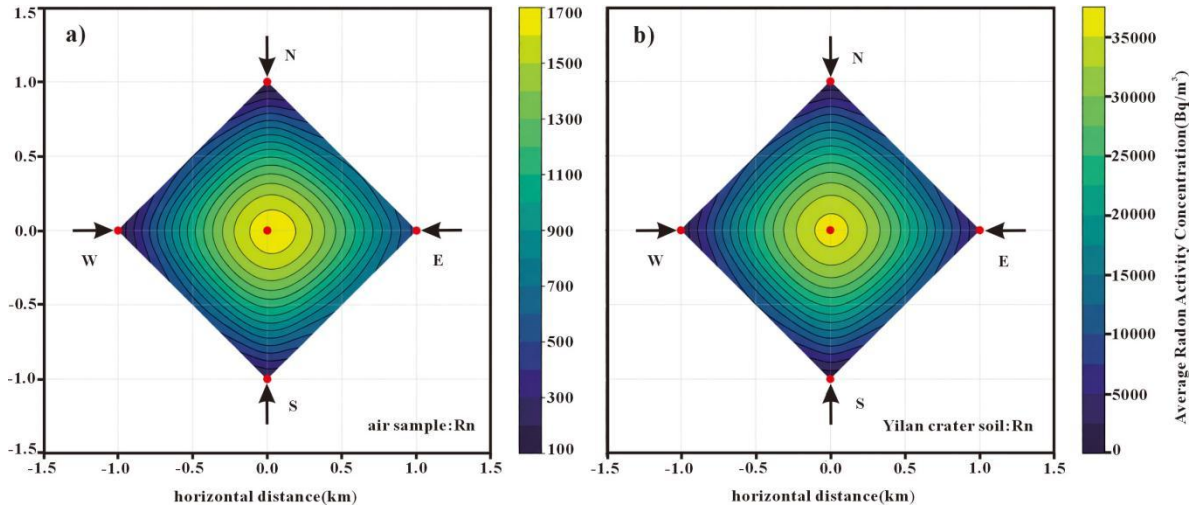


Figure 2 Distribution of air and soil radon concentrations in a certain impact crater in China

(a: Air radon concentration in the crater; b: Soil radon concentration in the crater)

Genetic Controlling Factors for Radon Distribution

The studied crater developed in Cretaceous granitic bedrock that commonly contains relatively high levels of primordial radionuclides; the crater rim diameter is 1850 m, with an average depth of 260 m from the rim crest to the crater floor[3]. Drilling core retrieved approximately 400 m southeast of the core reveals widespread planar deformation features (PDFs) within fused impact breccia (Fig. 3), corresponding to a ~120 m-diameter granitic projectile impacting at a vertical velocity of 12 km/s[21]. The hypervelocity impact pulverized the granitic bedrock, increased the specific surface area of the breccia by approximately 3-5 times, and generated abundant interconnected fractures and pores, thereby reducing resistance to upward radon migration and promoting radon accumulation in near-surface sediments within the core depression. Semi-closed crater topography and surficial weathering further loosen near-surface regolith and accelerate radon exhalation and dispersion[22,23]. In addition to geological constraints, meteorological conditions may modulate seasonal radon fluctuations. Field sampling was performed during rainy weather, when rainwater filled shallow surface voids and marshes developed in the core depression; these conditions may have temporarily inhibited vertical radon escape and enriched radon in subsurface sediments. Post-rainfall evaporation may subsequently trigger rapid radon release and concentration oscillations.

Overall, combined effects of impact-induced rock fragmentation, pervasive fracture networks, semi-enclosed geomorphology and seasonal meteorological variation collectively govern the unique radon spatial pattern of the studied crater.

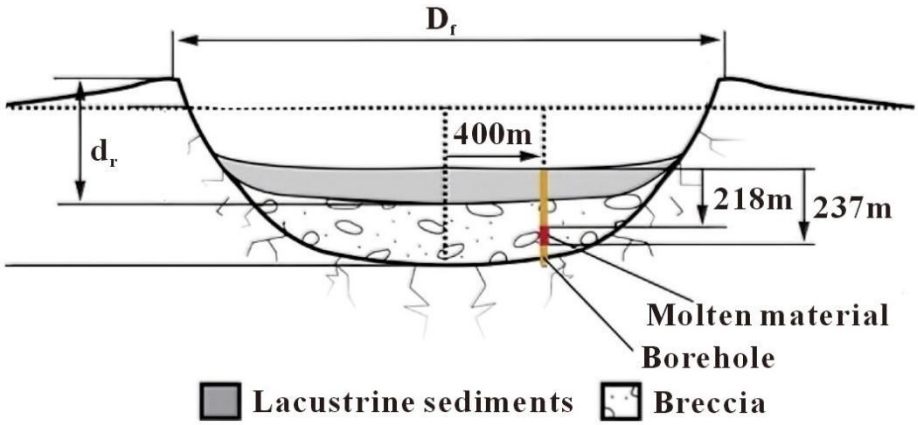


Figure 3 Schematic geological structure of a certain impact crater in China [21]

(Df: Rim diameter; dr: Average depth from crater rim to crater floor)

Spatial Variation of Primordial Radionuclides (^{232}Th, ^{40}K)

Spatial Differentiation of Radionuclide Specific Activity

The measured radionuclide activities showed the following general trends: inner rim > outer rim and granite > surficial sediment. (Appendix Table 1). The specific activity of ^{232}Th ranges from 12 to 69 Bq/kg: maximum value (69 Bq/kg) appears at east rim granite and outer rim granite reaches 61.5 Bq/kg, both lower than average ^{232}Th (112.48 ± 0.60 Bq/kg) of mineralized Homret Akarem granite pluton, Egyptian Nubian Shield[24] and consistent with 35-87 Bq/kg of Bergama-Kozak granodiorite, Turkey[25]. The minimum ^{232}Th (12 Bq/kg) occurs in east rim sediment, below average global terrestrial background (39.3 ± 0.8 Bq/kg) and regional soil range (42-88 Bq/kg) in western Turkey[25,26]. The ^{40}K activity varies between 669.3 and1330.3 Bq/kg: granitic values are far lower than Egyptian mineralized granite (3909.4 ±

37.56 Bq/kg) [24] and match 698-1100 Bq/kg of Turkish granodiorite[25]; sedimentary minimum of ^{40}K(669.3 Bq/kg) locates at east rim, close to lower limit of Turkish regional soil (667-1127 Bq/kg) and higher than global average terrestrial ^{40}K(375.3±10.2 Bq/kg), indicating that the 40K activity in this area remains within the natural background range and shows no obvious geochemical anomaly.

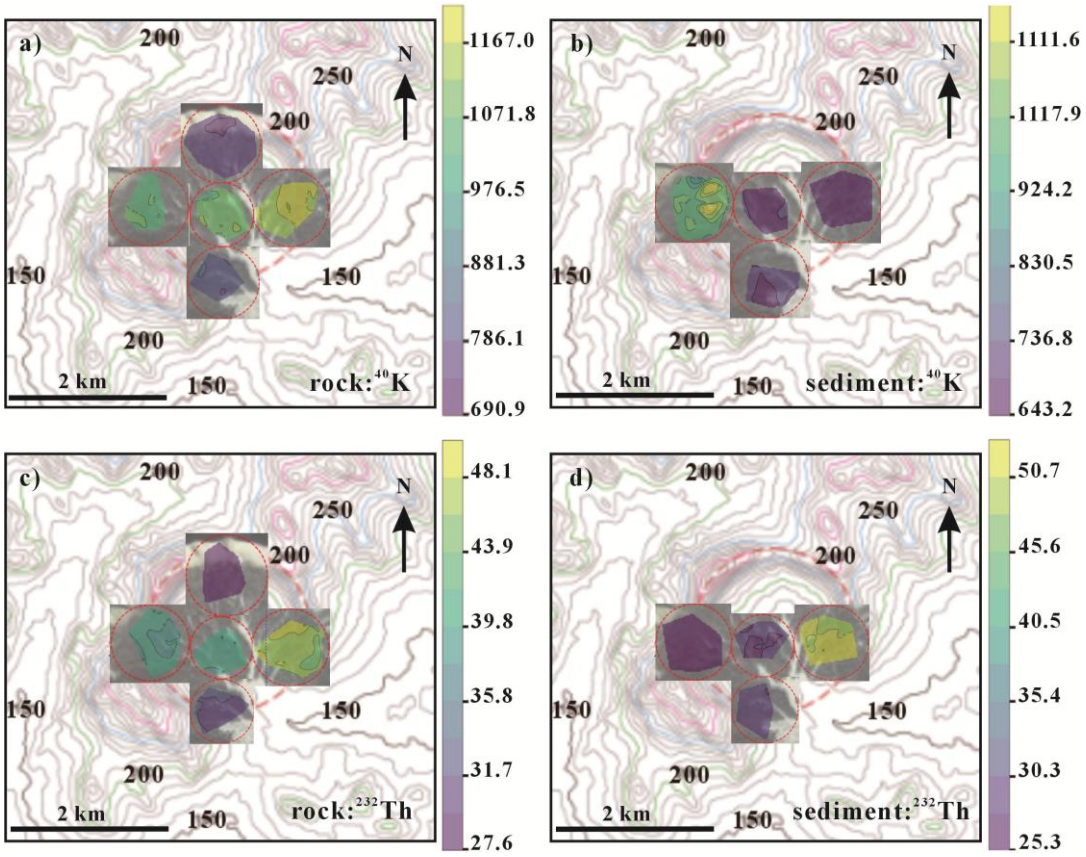


Figure 4 Distribution of radionuclide concentrations in a certain impact crater in China (a: ^{40}K concentration in granite of the crater; b: ^{40}K concentration in sediments of the crater; c: ^{232}Th concentration in granite of the crater; d: ^{232}Th concentration in sediments of the crater)

Interpolated distribution maps (Fig.4) show heterogeneous spatial enrichment: ^{40}K in granite shows localized high-value zones near the crater core and on both sides of the rim (>1071.8 Bq/kg, Fig.4a) controlled by original granitic potassium heterogeneity, while sedimentary ^{40}K high-value patches scatter more dispersedly with relatively lower magnitude (Fig.4b). Granite-hosted ^{232}Th concentrates dominantly at east rim (Fig.4c), whereas

sedimentary ^{232}Th high zone distributes sporadically at east rim with obvious depletion at core, south and west rim (Fig.4d); core and south rim exhibit synchronous variation trend of ^{40}K and ^{232}Th between granite and sediment.

Controlling Factors of Radionuclide Distribution

All measured ^{40}K and ^{232}Th activity concentrations fall within global natural background ranges, with no evidence of anomalous enrichment or depletion. Crater-fill deposits are mainly derived from the weathering of local Cretaceous granite and the reworking of impact breccia[3]. Potassium mainly incorporates into potassium feldspar and biotite while thorium concentrates within stable heavy accessory minerals (zircon, monazite), hence primary bedrock mineralogy is the fundamental constraint on baseline radionuclide abundance. The study area is dominated by physical weathering under mid-temperate semi-humid climate with limited chemical alteration[3]. During weathering, the relatively mobile ^{40}K is more susceptible to hydrological leaching and may become depleted in secondary sediments, whereas the less mobile ^{232}Th tends to remain near the source area or adsorb onto fine-grained sediments.[27,28].

Topographic gradient and catchment hydrology further modify element redistribution [29,30]: core depression serves as convergent sink for fine sediment with intensive leaching-induced K depletion and relatively homogeneous Th enrichment; steep north/south rim suffers strong surface erosion and uniformly low radionuclide content; gentle east/west rim preserves thicker sediment with intermediate radioelement concentration between core and steep slope. Grain-size discrepancy accounts for systematic activity difference between bedrock granite and overlying sediment. Global cross-comparison (Table 3) against published data from Croatia, Egypt, Turkey, India, Thailand and Nigeria [24,25,31-36] further confirms the studied crater's natural radioelement feature conforming to typical temperate granitic weathering crust background without anthropogenic or impact-related geochemical anomaly.

Table 3 Comparison of ^{40}K and ^{232}Th activity concentrations in a certain impact crater in China and other regions

Study area	Medium	^{40}K activity concentration (Bq/kg)	^{232}Th activity concentration (Bq/kg)
A certain impact crater in China	Granite	746.7–1330.3	40.9–69.0
Homret Akarem, Egyptian Nubian Shield [24]	Granitic pluton	3909.4 ± 37.56	112.48 ± 0.60
Bergama–Kozak, Turkey [25]	Granodiorite	698–1100	35–87
Gümüşhane City, northeastern Turkey [32]	Granite	62.6–1680.8; mean 638.5 ± 421.6	3.3–92.4; mean 33.5 ± 25.5
Bergama–Kozak, Turkey [25]	Soil	667–1127	42–88
Vransko Lake, Croatia [31]	Sediment	31–166	3.1–18
Northern Laptev Sea [36]	Marine sediment	—	17–36.3; 28.7–38.1
Faridkot and Mansa districts, India [33]	Soil	227.11–357.13; mean 312.76	61.01–142.34; mean 95.22
Southern Thailand nuclear power plant [34]	Surface soil	5–1422	6–170
Southwestern Nigeria [35]	Surface soil	34.9 ± 4.4–1358.6 ± 28.5; mean 286.5 ± 308.5	5.4 ± 1.1–502.0 ± 16.5; mean 91.1
a certain impact crater in China	Sediment	669.3–1001.5	12.0–40.6

Conclusions

The activity concentrations of ^{40}K and ^{232}Th in the studied impact crater fall within global natural background ranges. Their spatial distributions are jointly controlled by parent-rock composition, weathering and leaching, sedimentary processes, and topographic–hydrological conditions, reflecting the natural evolution of a granitic weathering–sedimentation system in an impact crater. Radon concentrations show a core-centered high-value pattern, which is mainly associated with intense impact-induced granite fragmentation and a well-developed interconnected fracture network in the crater center. Surface-water radon concentrations remain low, whereas sediments are identified as the predominant radon reservoir among the investigated media, including granite, air, and surface water. These results clarify the spatial distribution patterns and controlling mechanisms of natural radionuclides and radon under the influence of impact-induced structures, providing reference data for radiation environmental assessment and planetary geological studies of similar terrestrial impact craters.

Acknowledgements

This work was supported by the Projects Funded by the Natural Science Foundation of Heilongjiang Province (QC2025A008), Youth Innovation Fund Project of Heilongjiang Academy of Sciences (RC2026YZN04).

References

1. Guilmette R, Johnson N, Newton GJ et al (1991) Risks from radon progeny exposure: what we know, and what we need to know. Annu Rev Pharmacol Toxicol 31:513-539. https://doi.org/10.1146/annurev.pa.31.040191.003033

2. Othman SQ, Namq BF, Hussein ZA et al (2025) Radiological impact of primordial radionuclides and radon rates in rock-based building materials: Kurdistan region of Iraq. Environ Earth Sci 84:16. https://doi.org/10.1007/s12665-025-12468-x

3. Chen M, Xie X, Xiao W et al (2020) A certain impact crater in China, a newly identified impact structure. Chin Sci Bull 65:948-954. https://doi.org/10.1360/TB-2019-0704

4. Ioannides KG, Papachristodoulou C et al (1996) Measurements of ^{222}Rn migration in soil. J Radioanal Nucl Chem 208:541-547. https://doi.org/10.1007/BF02040071

5. Odumah H, KM, Opoku-Ntim I (2024) Indoor Radon Monitoring in Building Types of a Periurban Area in Cape Coast Metropolis, Southern Ghana. Indoor Air 2024. https://doi.org/10.1155/2024/8966193

6. Kumar A, Singh P, Singh D et al (2024) Assessment of exhalation rates of radon and thoron in soil from the Jaunsar-Bawar region of the Indian Himalayas. J Radioanal Nucl Chem 333:3147-3158. https://doi.org/10.1007/s10967-024-09407-8

7. Yasouka Y, Ishikawa T, Tokonami S et al (2007) A case study on the effect of water from groundwater sources on indoor radon levels. J Radioanal Nucl Chem 275:165-172. https://doi.org/10.1007/s10967-007-6956-y

8. Kerur BR, Rajeshwari T, Nagabhushna NM et al (2010) Radioactivity measurement in the granites of North Karnataka, India and its radiological implications. Indian J Phys 84:1467-1480. https://doi.org/10.1007/s12648-010-0139-3

9. Wang X, Luo L, Guo H et al (2013) Cratering process and morphological features of the Xiuyan impact crater in Northeast China. Sci China Earth Sci 56:1629-1638. https://doi.org/10.1007/s11430-013-4695-1

10. Alexeev VA, Gorin VD, Ivliev AI et al (2012) Integrated study of the thermoluminescence, noble gases, tracks, and radionuclides in the fresh-fallen Ash Creek L6 and Tamdakht H5 chondrites. Geochem Int 50:105-124. https://doi.org/10.1134/S0016702912020024

11. Vasconcelos MAR, Leite EP, Crosta AP (2012) Contributions of gamma-ray spectrometry to terrestrial impact crater studies: The example of Serra da Cangalha, northeastern Brazil. Geophys Res Lett 39:L04303. https://doi.org/10.1029/2011GL050525

12. Luo H, Deng YF, Zhang Z et al (2025) Shallow Structure Beneath a Certain Impact Crater in China Based on HVSR Analysis. Geotecton Metallog 49:900-911. https://doi.org/10.16539/j.ddgzyckx.2025.04.003

13. Czaja P (2022) Badania odbiorcze i eksploatacyjne instalacji fotowoltaicznych. Przegl Elektrotechn 12:52. https://doi.org/10.15199/48.2022.12.52

14. Darko EO, Adukpo OK, Fletcher JJ et al (2009) Preliminary studies on ^{222}Rn concentration in ground water from selected areas of the Accra metropolis in Ghana. J Radioanal Nucl Chem 283:507-512. https://doi.org/10.1007/s10967-009-0378-y

15. Yang XL, Ma H, Li ZY (2024) Study on Distribution Characteristics and Influencing Factors of Soil Radon Concentration in Shizuishan City, Ningxia. Geol Res Environ Prot 3:1-3. https://doi.org/10.37155/2811-0595-0307-1

16. Luna-Lucero ME, Sajo-Bohus L, Lopez JA (2023) Radon at Kilbourne Hole Maar and Magnetic and Gravimetric Correlations. Int J Environ Res Public Health 20:5185. https://doi.org/10.3390/ijerph20065185

17. Planinic J, Lokobauer N, Franic Z et al (1993) Radon dose in cellars during the war in Croatia. J Radioanal Nucl Chem 176:91-101. https://doi.org/10.1007/BF02163189

18. Salim LA, Bonotto DM (2019) Radon exhalation rate and indoor exposure in a Brazilian coal mine. J Radioanal Nucl Chem 320:587-595. https://doi.org/10.1007/s10967-019-06531-8

19. Malakootian M, Khashi Z, Iranmanesh F et al (2014) Radon concentration in drinking water in villages nearby Rafsanjan fault and evaluation the annual effective dose. J Radioanal Nucl Chem 302:1167-1176. https://doi.org/10.1007/s10967-014-3345-1

20. Tabar E, Yakut H (2013) Radon measurements in water samples from the thermal springs of Yalova basin, Turkey. J Radioanal Nucl Chem 299:311-319. https://doi.org/10.1007/s10967-013-2845-8

21. Ren JK, Zhang QM, Liu WJ et al (2023) Numerical simulation of the formation process of a certain impact crater in China. Explos Shock Waves 43:115-125. https://doi.org/10.11883/bzycj-2022-0115

22. Sun X, Yang P, Xiang Y et al (2018) Across-fault distributions of radon concentrations in soil gas for different tectonic environments. Geosci J 22:227-239. https://doi.org/10.1007/s12303-017-0028-2

23. Wilkening MH, Rust WD (1972) Radon-222 concentrations in a mountain canyon environment. Meteorol Atmos Phys 21:183-194. https://doi.org/10.1007/BF02247971

24. Heikal MThS, Shereif AS, Azer MK (2024) Gamma activity concentrations (^{226}Ra, ^{232}Th, ^{40}K) of mineralized Homret Akarem composite granitic pluton, Egyptian Nubian Shield: environmental hazards assessment. Euro-Mediterr J Environ Integr 9:1629-1658. https://doi.org/10.1007/s41207-024-00589-x

25. Karadeniz O, Ciyrak N, Yaprak G et al (2011) Terrestrial gamma exposure in the granodiorite area of Bergama (Pergamon) – Kozak, Turkey. J Radioanal Nucl Chem 288:919-926. https://doi.org/10.1007/s10967-011-1031-0

26. Altikulac A, Turhan S, Gumus H (2015) Activity concentration of terrestrial and anthropogenic radionuclides (^{226}Ra, ^{222}Rn, ^{232}Th, ^{40}K, and ^{137}Cs) in soil samples. Environ Earth Sci 75:1. https://doi.org/10.1007/s12665-015-4841-5

27. Jarvis AGMJ (2004) Dynamics of potassium leaching on a hillslope grassland soil. J Environ Qual 33:1920-1927. https://doi.org/10.2134/jeq2004.1920

28. Kovacheva P, Mitsiev S, Djingova R (2013) Physicochemical fractionation of americium, thorium, and uranium in Chernozem soil after sharp temperature change and soil drought. Chem Pap 68:336-341. https://doi.org/10.2478/s11696-013-0457-y

29. Krishnamoorthy N, Mullainathan S, Mehra R (2015) Variation of naturally occurring radionuclides, dose rate and mineral characteristics with particle size and altitude in bottom sediments of a river originating from Anamalai hills in the Western Ghats of India. Environ Earth Sci 74:3467 – 3483. https://doi.org/10.1007/s12665-015-4382-y

30. Krishnamoorthy N, Mullainathan S, Chaparro MAE et al (2017) Potential effect of natural radionuclides in riverbed sediments: a statistical approach based on granulometric and magnetic mineral differences. Environ Earth Sci 76:397. https://doi.org/10.1007/s12665-017-6606-9

31. Fajkovic H, Mikelic LLI, Prohic E (2012) Vertical distribution of ^{40}K, ^{232}Th, and ^{137}Cs mass activities in lake sediment (Vransko Lake, Croatia) and their relationship with the source material and sedimentation. J Radioanal Nucl Chem 295:2273-2282. https://doi.org/10.1007/s10967-012-2332-7

32. Maden N, Akaryali E, Celik N (2019) The in situ natural radionuclide (^{238}U,^{232}Th and ^{40}K) concentrations in Gümüşhane granitoids: implications for radiological hazard levels of Gümüş hane city, northeast Turkey. Environ Earth Sci 78:386. https://doi.org/10.1007/s12665-019-8333-x

33. Mehra R, Singh S, Singh K (2009) Analysis of ^{226}Ra, ^{232}Th and ^{40}K in soil samples for the assessment of the average effective dose. Indian J Phys 83:1031-1037. https://doi.org/10.1007/s12648-009-0064-5

34. Kritsananuwat R, Arae H, Fukushi M et al (2015) Natural radioactivity survey on soils originated from southern part of Thailand as potential sites for nuclear power plants from

radiological viewpoint and risk assessment. J Radioanal Nucl Chem 305:487-499. https://doi.org/10.1007/s10967-015-3994-8

35. Ajayi OS (2009) Measurement of activity concentrations of ^{40}K, ^{226}Ra and ^{232}Th for assessment of radiation hazards from soils of the southwestern region of Nigeria. Radiat Environ Biophys 48:323-332. https://doi.org/10.1007/s00411-009-0225-0

36. Domanov MM, Gagarin VI, Bukhanov MV (2023) Features of ^{226}Ra, ^{232}Th, ^{238}U Distribution in the Surface Layer of Bottom Sediments in the Northern Part of the Laptev Sea. Radiochemistry 64:766 – 775. https://doi.org/10.1134/S1066362222060145

Supplementary Files

This is a list of supplementary files associated with this preprint. Click to download.

- Supplementarymaterial.xlsx